

LA-UR-18-29418 (Accepted Manuscript)

## Structural representation of additively manufactured 316L austenitic stainless steel

Bronkhorst, Curt Allan  
Mayeur, Jason Rhea  
Livescu, Veronica  
Brown, Donald William  
Gray, George Thompson III  
Vander Wiel, Scott Alan

Provided by the author(s) and the Los Alamos National Laboratory (2019-05-09).

**To be published in:** International Journal of Plasticity

**DOI to publisher's version:** 10.1016/j.ijplas.2019.01.012

**Permalink to record:** <http://permalink.lanl.gov/object/view?what=info:lanl-repo/lareport/LA-UR-18-29418>

**Disclaimer:**

Los Alamos National Laboratory, an affirmative action/equal opportunity employer, is operated by Triad National Security, LLC for the National Nuclear Security Administration of U.S. Department of Energy under contract 89233218CNA000001. By approving this article, the publisher recognizes that the U.S. Government retains nonexclusive, royalty-free license to publish or reproduce the published form of this contribution, or to allow others to do so, for U.S. Government purposes. Los Alamos National Laboratory requests that the publisher identify this article as work performed under the auspices of the U.S. Department of Energy. Los Alamos National Laboratory strongly supports academic freedom and a researcher's right to publish; as an institution, however, the Laboratory does not endorse the viewpoint of a publication or guarantee its technical correctness.

# Accepted Manuscript

Structural Representation of Additively Manufactured 316L Austenitic Stainless Steel

C.A. Bronkhorst, J.R. Mayeur, V. Livescu, R. Pokharel, D.W. Brown, G.T. Gray, III

PII: S0749-6419(18)30765-4

DOI: <https://doi.org/10.1016/j.ijplas.2019.01.012>

Reference: INTPLA 2477

To appear in: *International Journal of Plasticity*

Received Date: 20 November 2018

Revised Date: 26 January 2019

Accepted Date: 26 January 2019

Please cite this article as: Bronkhorst, C.A., Mayeur, J.R., Livescu, V., Pokharel, R., Brown, D.W., Gray III., G.T., Structural Representation of Additively Manufactured 316L Austenitic Stainless Steel, *International Journal of Plasticity*, <https://doi.org/10.1016/j.ijplas.2019.01.012>.

This is a PDF file of an unedited manuscript that has been accepted for publication. As a service to our customers we are providing this early version of the manuscript. The manuscript will undergo copyediting, typesetting, and review of the resulting proof before it is published in its final form. Please note that during the production process errors may be discovered which could affect the content, and all legal disclaimers that apply to the journal pertain.



## Structural Representation of Additively Manufactured 316L Austenitic Stainless Steel

C. A. Bronkhorst<sup>1\*</sup>, J. R. Mayeur<sup>3</sup>, V. Livescu<sup>2</sup>  
R. Pokharel<sup>2</sup>, D. W. Brown<sup>2</sup>, G. T. Gray III<sup>2</sup>

<sup>1</sup>Department of Engineering Physics  
University of Wisconsin – Madison  
Madison, WI 53706 USA

<sup>2</sup>Materials Science and Technology Division  
Los Alamos National Laboratory  
Los Alamos, NM 87545 USA

<sup>3</sup>Department of Mechanical and Aerospace Engineering  
University of Alabama in Huntsville  
Huntsville, AL 35899 USA

### ABSTRACT

Three 316L stainless steel materials are studied and reported upon; wrought, as-built additively manufactured (AM), and heat-treated AM material. The AM material was produced from the laser engineered net shaping (LENS) process. Macroscopic uniaxial compression stress-strain curves were obtained for all three materials. The curves were similar for the wrought and heat-treated AM materials but the as-built AM material demonstrated approximately 1.7 times greater flow stress at any given level of strain than the other two materials. Electron-backscatter diffraction analysis of the materials also showed that the microstructures of the three materials differed; with complex grain morphology for the as-built AM material. The mean grain size of each of the three materials also differed. The initial dislocation density was also measured with neutron diffraction and line-profile analysis for both wrought and as-built AM materials with the density in the AM material approximately 2.5 times greater. A single crystal model was proposed to represent the essential features of the three FCC materials accounting for dislocation interactions and representation of grain size via a simple Hall-Petch type term. The strength of this term is evaluated through independent experimental results on traditionally manufactured materials. The model was applied to each of the three materials by simulation of the uniaxial compression experiments by direct numerical simulation of electron-backscatter diffraction images. This allowed for representation of the size of each grain in the simulations. The results suggest that the difference in initial dislocation density of the three materials is the primary factor causing the difference in stress-strain response. Although the differences in grain size contribute to a higher stress for the as-built AM material, the effect is small. Other factors such as internal stress and grain morphology could play a role in mechanical behavior difference and these two factors are also discussed.

---

\* Corresponding author. E-mail address: cbronkhorst@wisc.edu  
LA-UR-18-29418

**Keywords:** Additive manufacturing, plastic slip, dislocation density, flow stress, polycrystal plasticity, stainless steel.

## 1. Introduction

The metal additive manufacturing (AM) processes being offered commercially at the present time are diverse - with combinations of process type and equipment manufacturer (Gao, 2015; Frazier, 2014; Guo, 2013). Each of these variations will have the potential to produce materials of differing characteristics (Wang *et al.*, 2016; Yang *et al.*, 2017). In addition, the process conditions and component geometry add an additional source of variation to the characteristics of the material produced by any given AM system (Morrow *et al.*, 2018). It has been clearly demonstrated that the materials produced from AM processes are unique to our prior mechanics experience (Bartolomeu, 2017; Lou, 2017; Lu *et al.*, 2018; Marya *et al.*, 2015; Nishida *et al.*, 2015; Pham *et al.*, 2017; Martin *et al.*, 2017). The individual grain morphologies differ significantly from the traditionally manufactured and annealed metallic materials (Gray *et al.*, 2017; Chen *et al.*, 2017, 2018; Guo *et al.*, 2017; Lim *et al.*, 2015; Pace *et al.*, 2017; Zhong, 2017; Li and Tan, 2018). Traditionally manufactured thermo-mechanically processed metallic materials have grain topologies which are generally equiaxed and reasonably isotropic. Rolling or extrusion processing steps are capable of rendering both morphological and crystallographic texture to the material, however those anisotropies are usually relatively uniform throughout the component. This is certainly not the case in general for additively manufactured materials (Livescu *et al.*, 2018). Processing conditions and build patterns can play a significant role in influencing the mechanical response of the as-built material (Brown *et al.*, 2017, 2018). The build pattern plays a significant role in determining mechanical response since there are two characteristic structural features within the as-built materials – the “weld” bead and the single crystal (Rännar *et al.*, 2017; Wang *et al.*, 2018). Each is readily observable in as-built materials and the crystallographic morphology of grains within each “bead” is determined by the processing and solidification conditions. The morphology of grains can be quite complex – far outside our experience in representing the micro-mechanics of deformation for such materials (Francois *et al.* 2017; Tapia *et al.*, 2017; Livescu *et al.*, 2018).

The attractiveness of using additively manufacturing components for applications is the ability to produce complex shaped parts – which could not be produced through casting or subtractive machining procedures alone (e.g. Bonatti and Mohr, 2017). In practice, an additively manufactured component generally requires some modest subtractive machining for surface finish or dimensional specification reasons. However, much of the component will have been produced by AM. With this complexity in part topology, the conditions (e.g. laser energy, build pattern, cooling rate) of the material production at different locations within the component have the potential to vary greatly (Wang *et al.*, 2016). With these differing conditions comes the possibility that the characteristics and properties of the material will also vary greatly within a single produced component. This could mean that “weld” bead size and grain size and morphology could change with position within the part. This is illustrated in the micrograph images given in Fig. 1. In addition, the initial dislocation state of the material could also be variable (Pokharel *et al.*, 2018; Brown *et al.*, 2017, 2018). For structural applications then, the plastic flow resistance of the material could vary substantially (> 10%) at different locations

within the part (Gray *et al.*, 2017; Guo *et al.*, 2017; Yadollahi *et al.*, 2016; Wang *et al.*, 2016). It has been demonstrated that there is a residual internal stress state in these parts upon cooling. This is true both at the part scale and the scale of the microstructure (Strantz *et al.*, 2018; Wu *et al.*, 2014; Kapoor *et al.* 2018; Simson *et al.* 2017). This internal stress state then could also potentially vary spatially. For traditionally manufactured materials, the single crystal was the primary microstructural constituent that dictated the variability in stress state and damage response of the material. For AM materials, the single crystal remains an essential structural feature of the material, however there are now AM weld beads that add an additional morphological length scale to the material microstructure. In terms of internal material interfaces, not only are there grain boundaries to consider, but also the interbead regions or interfaces which are as yet poorly understood and subject to the same variability due to varying process conditions (Gray *et al.*, 2017; Yadollahi *et al.* 2016). Through post-processing heat treatment it may be possible to alleviate these spatial variations for some components, however with residual internal stress, there is a potential to also change the dimensions of the part once heated and re-cooled. Although we do not explicitly account for the possible effect of residual internal stress in our results, we do consider its potential influence in the discussion.

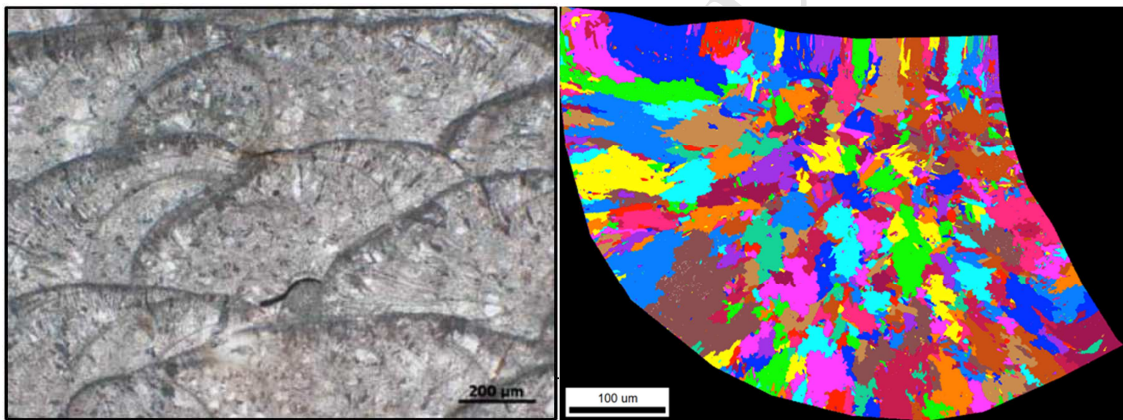


**Fig. 1.** The light micrograph image to the left shows individual weld beads in a build of 304L stainless steel. The EBSD image to the right shows an example of a single weld bead with complex and location dependent grain morphology.

The influence of grain size on the plastic flow resistance is well known, but that experience is based upon the traditionally manufactured material. The well-known empirically based Hall-Petch expression for characterizing the relationship between mean grain size and flow stress of a material is based upon material of a traditional structure (Cordero *et al.*, 2016; Feaugas and Haddou, 2003; Kashyap and Tangri, 1995; Singh *et al.*, 2002). Our understanding of grain boundary influence on mechanical behavior is not yet good enough to generalize the influence of grain size to plastic flow resistance of the materials of vastly differing structures such as AM produces (Livescu *et al.*, 2018). It has also become clear that AM processes produce states of dislocation structure that differ greatly from an annealed state (Wang *et al.*, 2016). The result of this structure is manifest in significantly greater plastic flow resistance for the as-built materials in comparison to annealed material. In addition, each process condition has the potential to produce material with differing initial structure and hence significantly different mechanical behavior. Building alloys also introduces the possibility for alloying chemistry variability, either

by design or accident. Finally, each given AM system may be used to build components of differing alloy composition (e.g. AlMangour, 2017; Zhong *et al.*, 2017). With this opportunity also brings with it the possibility for un-intended chemical elements to invade a given component build and for impurities to be introduced during the build process.

The Laser Engineered Net Shaping (LENS) process of metal additive manufacturing was used to manufacture the sample material used for the work presented here (Gray *et al.*, 2017). This process employs a powder feed system, which guides a flow of metal powder to the point of the sample surface containing the melt pool produced by the laser. Generally, multiple feed ports are directed along the axis of the laser within the vertically mounted laser head. The sample is produced on a build plate that is mounted on an X-Y table that traverses within the plane of the table in concert with the laser head. The laser head then moves in the Z direction as the part builds in dimension. During processing the laser head is generally encased with a flow of inert gas to prevent excess influence from ambient oxygen and facilitate surface wetting. More details of the particular processing conditions used for this work are given below in the experimental section.

Given the many outstanding questions surrounding the nature of additively manufactured metallic materials outlined above, the general performance certification for structural application of these new class of materials remains a very large challenge (e.g. Francois *et al.*, 2017). This also implies challenges in numerically representing these materials within engineering simulations during design or performance evaluation when plastic deformation and especially damage assessment may be of interest (Gray *et al.*, 2018; Yadollahi *et al.*, 2016). Although the commonly used  $J_2$  plasticity theories that employ traditional strength models remain largely phenomenological in character, the progression of single crystal models over the past several years has been towards a greater physical basis (e.g. Gurtin *et al.* 2010; Cheong and Busso, 2004; Grilli *et al.*, 2018; Knezevic and Beyerlein, 2018; Hansen, *et al.*, 2013; Feng *et al.*, 2018; Haouala *et al.*, 2018; Dequiedt *et al.*, 2015; Kubin, 2013; Wang *et al.*, 2017). The use of dislocation density rather than flow stress as the primary evolutionary state variable has facilitated a greater capability in predicting dislocation slip based plasticity behavior. This progression has also opened a great many opportunities to better couple with advanced experimental techniques for measurement of dislocation state and results from discrete dislocation dynamics calculations in a quantitative way. Recently, continuum theories of dislocation slip have moved from the traditional scalar scaling factor for simple forest hardening to a tensorial representation where specific interactions between dislocations on each slip system and between the slip systems can be defined (e.g. Dequiedt *et al.* 2015; Grilli *et al.* 2018; Kubin, 2013). This affords an additional level of physical accuracy in hardening behavior and also begins to open up the potential to calculate dislocation sub-structure development. The latter has long been lacking in continuum single crystal theories and the ability to more quantitatively predict intra-granular deformation behavior. We will employ an advanced model for FCC materials here with the goal of describing the deformation response of AM materials and interpreting the underlying physical response.

Our experience to date with AM is that the morphology of grains within the as-built materials is far from equiaxed. Although indications are that process conditions weigh heavily on the microstructure that is developed and there is yet much to be learned, the grain shape in many

examples of AM produced materials is very complex. The occurrence of highly elongated grains is very possible and flat surface grain boundaries are less probable. The influence of grain morphology has to some extent been explored but not as much as that of crystallographic texture. In our development of models for representation of this new class of material, we must then be mindful that there is still much we do not know and therefore cannot represent about the role of grain boundaries in the structural response of AM materials. In the work presented here, we employ a simple representation of the influence of grain size of plastic flow resistance. This is done as an early representation of the influence of grain size in order to quantitatively understand the role of different mechanisms on flow stress differences between AM materials and more traditionally manufactured materials.

The manuscript will continue in section 2 by describing the processing history of the three different materials examined in this study. Section 3 will present the experimental results from those conducted on the three materials. In section 4 the single crystal model is defined and described in the context of this study. Section 5 contains the description of material parameter evaluation and the sources of information used during that process. The simulations performed are described in section 6 along with comparisons to experiments and uncertainty assessment. The results are discussed in section 7 and we will conclude with some final thoughts in section 8.

## 2. Experimental Results

The material being considered in this study was manufactured using a LENS MR-7 laser AM system from Optomec (Albuquerque, NM) as described in a publication by Gray *et al.* (2017). The details of the commercially available wrought plate material used as the reference in this study were also reported upon by Gray *et al.* (2017). In addition to the plate and as-built AM materials, a portion of the as-built material was heat-treated to 1060° C for one hour under vacuum followed by cooling to room temperature in 2 ½ minutes by rapid Argon gas quenching with the intent to fully recrystallize the AM microstructure. Electron backscatter diffraction (EBSD) and light optical microscopy (LOM) were utilized to investigate the microstructures of the three starting 316L SS materials. Representative images of the microstructures for all three materials are given in Fig. 2. All AM samples were produced as right-circular cylinders 25 mm diameter and 33 mm tall.

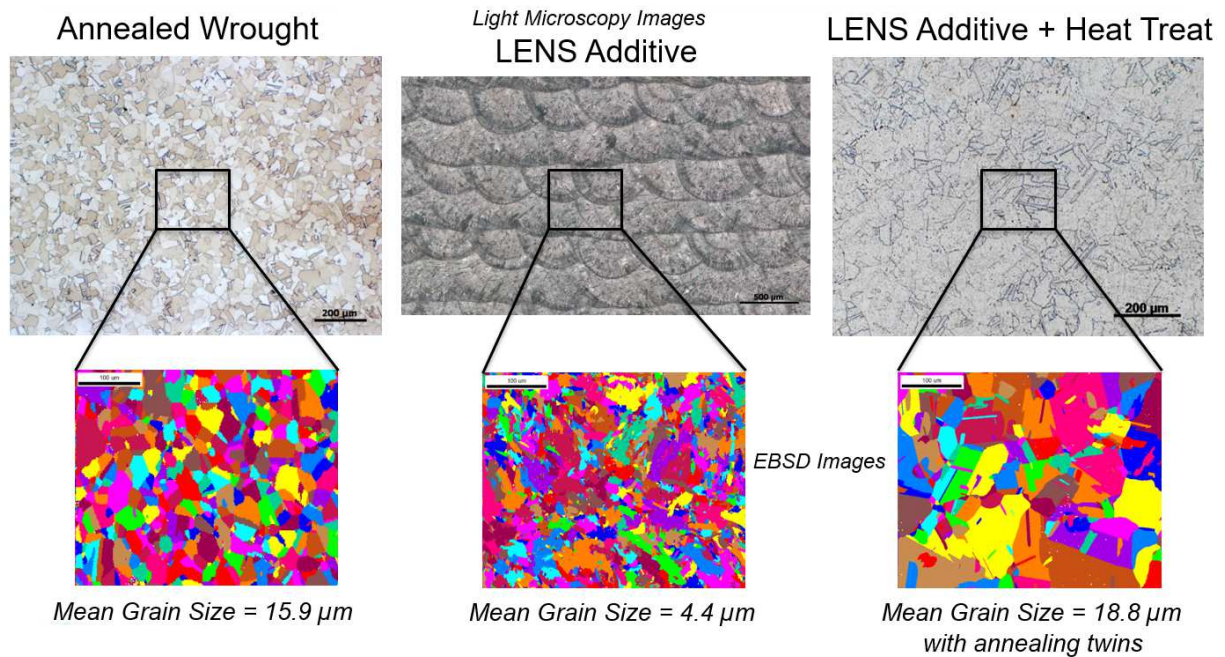


**Fig. 2.** LOM and EBSD images of the three materials considered in this study. The scale and relative position of each EBSD image are shown in the figure.

Simple compression experiments were also conducted on each of the three materials by electro-machining cylindrical samples of 5 mm diameter and 5 mm tall. Quasi-static compression tests were conducted using an Instron screw-driven test system at a strain rate of  $0.001 \text{ s}^{-1}$  and temperature of 298 K and the stress-strain curves for those experiments are given in Fig. 3. The simple compression experiments performed on the wrought material also included a strain rate jump from  $0.001 \text{ s}^{-1}$  to  $0.1 \text{ s}^{-1}$ , which is apparent from the black curves in Fig. 3. Once again, the details of the experiments can be found in Gray *et al.* (2017). A number of replicate compression experiments were conducted on each of the three materials. The loading direction for the AM materials was along the build axis (Z direction) of the manufactured cylinders.

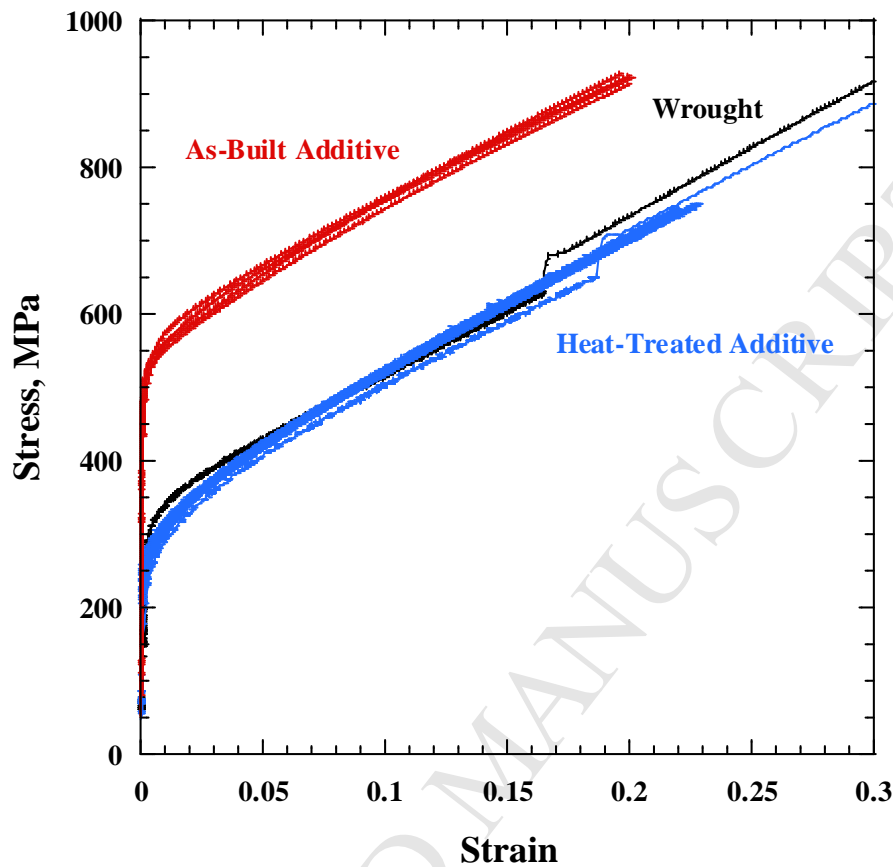


**Fig. 3.** Stress-strain response of the three materials considered here. The data represented is taken from Gray *et al.* (2017). The red curves are those of the as-built AM material, the blue curves those of the heat-treated AM material, and the black curves are from the wrought material.

The wrought and as-built AM materials were probed by *in situ* neutron diffraction measurements using the procedures outlined in Brown *et al.* (2017). These measurements were conducted on the Spectrometer for Materials Research at Temperature and Stress (SMARTS) at the Lujan Center at the Los Alamos Neutron Science Center (LANSCE) in order to carry out diffraction line profile analysis on both materials. The diffraction patterns collected during heat treating were analyzed with Rietveld refinement of the full pattern using the General Structural Analysis Software (GSAS) to determine the lattice parameter, phase fraction and peak variance. Quantitative diffraction line profile analysis was completed using the extended Convolutional Multiple Whole Profile (eCMWP) line profile analysis method (Ribarik *et al.*, 2004).

The diffraction intensity profile is affected by the lattice distortion caused by the presence of dislocations in the material. A higher level of lattice distortion will generally lead to the broadening of the lattice diffraction peaks due to the variability in lattice dimensions caused by that dislocation distortion. An analysis of the line profiles for an estimate of the structural state of the material begins by calculating theoretical profile functions as the convolution of the

theoretical size, distortion, and planar fault profiles and measured instrumental profiles which have the characteristics of the microstructure as parameters. These theoretical profiles are based on physical models, which describe the effect of size, dislocations, and faulting on the shape of the diffraction profiles. The profile functions are fitted to the full measured pattern by a non-linear, least-squares algorithm through which the parameters of the microstructure are determined. The dislocation density was determined from the diffraction data collected in the high-angle, high-resolution, detector on SMARTS. The (002) peak for both the wrought and as-built AM materials are given in Fig. 5 to highlight the peak broadening observed in the AM material. The dislocation density from these line profiles were determined to be  $9.0 \times 10^7 \text{ mm}^{-2}$  and  $2.3 \times 10^8 \text{ mm}^{-2}$  for the wrought and AM materials respectively. Dislocation density measurements were not made on the annealed materials but were assumed to have an initial dislocation density that of the annealed wrought material.

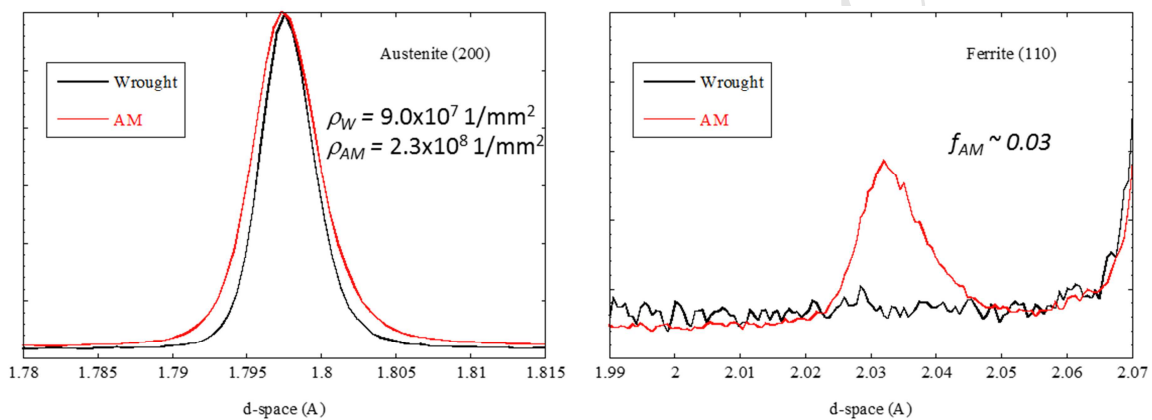


**Fig. 4.** Neutron diffraction lattice spacing profile for both the wrought material and the as-built additively manufactured material with estimates of dislocation density. The right-hand profile gives an estimate of the ferrite content in the as-built AM material of 3%. The black curves are those from the wrought material and the red curves from the as-built AM material.

In-situ measurements during heat treating were made on both materials on the lower resolution detector bank (bank 1) to glean the ferrite fraction quantitatively and the dislocation density qualitatively. Each material was heated to a temperature of  $1050 \text{ }^\circ\text{C}$  at a rate of  $10 \text{ }^\circ\text{C/min}$ , and then cooled to room temperature at the same rate, while diffraction data was collected. For each material, the full-width half maximum (FWHM) of the (200) peak is shown as a function of temperature in Fig. 5. Initially, the AM material exhibits a broader peak consistent with Fig. 4 which is associated with a high dislocation density. With heating, the breadth of the peak from the AM material decreases sharply between  $720 \text{ }^\circ\text{C}$  and  $800 \text{ }^\circ\text{C}$  indicative of dislocation recovery. Unfortunately, the same range of data was lost during the heat treating of the wrought sample because of an accelerator failure. High resolution measurements (bank 3) after the completion of the heat treatment exhibited peaks consistent with the instrumental resolution, that is the dislocation density was below the detection limit of  $\sim 1.0 \times 10^7 \text{ mm}^{-2}$ . A thermal expansion coefficient of  $16.2 \text{ } \mu\text{m/m-K}$  for the 316L material was measured.

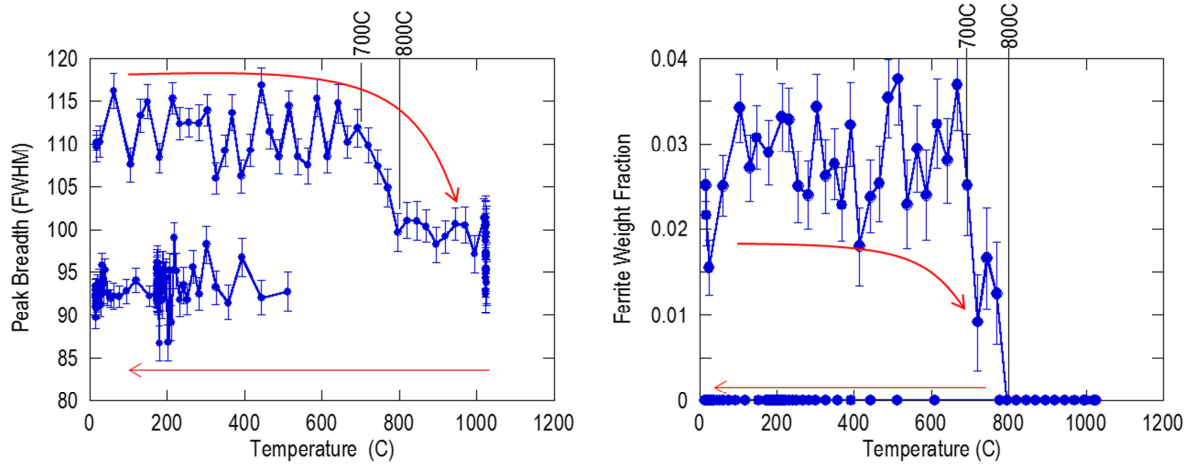


**Fig. 5.** Line profile peak width and ferrite fraction as a function of temperature for the thermal cycle imposed on the as-built additively manufactured material.

### 3. Single Crystal Model

The historical basis for the single crystal constitutive model presented here can be found in the works by Rice (1971), Hill and Rice (1972), Asaro and Rice (1977), Asaro *et al.* (1983a,b), Kocks *et al.* (1975), Kalidindi *et al.* (1992), Bronkhorst *et al.* (1992), Anand (2004), Bronkhorst *et al.* (2007), Alleman *et al.* (2015). Within the deformation rates examined here, the coupled thermo-mechanical elasto-viscoplastic formulation assumes that thermally activated slip is the dominant mechanism for plastic deformation.

The kinematics are defined such that the deformation gradient is decomposed into reference, intermediate (iso-clinic), and current configurations. Therefore, the deformation gradient decomposition is correspondingly given by

$$\mathbf{F} \equiv \mathbf{F}^* \mathbf{F}^p, \quad (1)$$

where it is assumed that

$$\det \mathbf{F}^* > 0; \quad \det \mathbf{F}^p = 0. \quad (2)$$

Lattice rotation is contained within the elastic deformation,  $\mathbf{F}^*$ , therefore the slip system direction vector  $\mathbf{m}_0^\alpha$  and slip system normal vector  $\mathbf{n}_0^\alpha$  defined in the reference configuration are defined in the current deformed configuration as

$$\mathbf{m}^\alpha = \mathbf{F}^* \mathbf{m}_0^\alpha; \quad \mathbf{n}^\alpha = \mathbf{F}^{*-T} \mathbf{n}_0^\alpha. \quad (3)$$

The constitutive model is defined in the intermediate configuration and therefore the second Piola-Kirchoff stress is given by

$$\mathbf{T}^* = \underline{\underline{\mathcal{L}}}(\theta) [\mathbf{E}^* - \mathbf{A}(\theta - \theta_0)] , \quad (4)$$

where  $\theta$  is temperature,  $\theta_0$  is the reference temperature,  $\underline{\underline{\mathcal{L}}}(\theta)$  is the fourth order elastic stiffness tensor as a function of temperature, and  $\mathbf{A}$  is the thermal expansion tensor. The elastic Green-Lagrange strain  $\mathbf{E}^*$  in the intermediate configuration is given by

$$\mathbf{E}^* \equiv \frac{1}{2} (\mathbf{F}^{*T} \mathbf{F}^* - \mathbf{1}) . \quad (5)$$

The second Piola-Kirchoff stress is related to the Cauchy stress,  $\mathbf{T}$  in the current configuration by

$$\mathbf{T}^* = \mathbf{F}^{*-1} (\det \mathbf{F}^*) \mathbf{T} \mathbf{F}^{*-T} . \quad (6)$$

The plastic velocity gradient,  $\mathbf{L}^p$  is defined in relation to the slip rate on the collection of slip systems  $\dot{\gamma}^p$  by

$$\mathbf{L}^p = \dot{\mathbf{F}}^p \mathbf{F}^{p-1} = \sum_{\alpha} \dot{\gamma}^{\alpha} \mathbf{S}_0^{\alpha} , \quad (7)$$

where the Schmid tensor  $\mathbf{S}_0^{\alpha}$ , defining the geometry of each of the 12  $\{111\}\langle 110 \rangle$  slip systems  $\alpha$  is given by

$$\mathbf{S}_0^{\alpha} = \mathbf{m}_0^{\alpha} \otimes \mathbf{n}_0^{\alpha} . \quad (8)$$

The shear rate due to dislocation slip is defined on each slip system  $\alpha$  by an expression representing the thermally activated motion of dislocations (Kocks *et al.*, 1975; Busso, 1990; Cheong and Busso, 2004)

$$\dot{\gamma}^{\alpha} = \dot{\gamma}_0 \exp \left[ -\frac{F_0}{k\theta} \left\langle 1 - \left\langle \frac{|\tau^{\alpha}|}{\frac{\mu(\theta)}{\mu_0} (s_{\rho}^{\alpha} + s_l^{\alpha})} \right\rangle \right\rangle^p \right] \text{sgn}(\tau^{\alpha}) , \quad (9)$$

where  $\dot{\gamma}_0$  is a constant strain rate factor,  $F_0$  is activation energy,  $k$  is Boltzman's constant,  $\mu$  is the temperature dependent shear modulus,  $\mu_0$  is the reference shear modulus at 0 K,  $s_{\rho}^{\alpha}$  is the deformation resistance stress due to dislocation structure,  $s_l^{\alpha}$  is the intrinsic lattice resistance,

and  $p$  and  $q$  are exponents to determine the shape of the energy barrier for dislocation motion. The resolved shear stress is given by the following expression

$$\tau^\alpha = (\mathbf{C}^* \mathbf{T}^*) \cdot \mathbf{S}_0^\alpha \approx \mathbf{T}^* \cdot \mathbf{S}_0^\alpha, \quad (10)$$

where

$$\mathbf{C}^* = \mathbf{F}^{*T} \mathbf{F}^*. \quad (11)$$

The shear modulus is given by

$$\mu(\theta) = \sqrt{C_{44}(\theta) \left( \frac{C_{11}(\theta) - C_{12}(\theta)}{2} \right)}, \quad (12)$$

where

$$C_{ij}(\theta) = C_{ij0} + m_{ij} \theta. \quad (13)$$

The resistance stress due to grain size and dislocation structure is given by

$$s_\rho^\alpha = s_\infty + \frac{k_{gr}}{\sqrt{d_{gr}}} + \mu b \sqrt{\sum_\beta a^{\alpha\beta} \rho^\beta}. \quad (14)$$

where  $b$  is Burger's vector,  $k_{gr}$  is the grain size factor,  $s_\infty$  is a far field resistance,  $d_{gr}$  is mean grain diameter,  $a^{\alpha\beta}$  is the dislocation interaction tensor, and  $\rho^\beta$  is dislocation density on slip system  $\beta$ .

The interaction tensor has been developed over some time for FCC materials (Dequiedt *et al.*, 2015; Kubin, 2013; Madec *et al.*, 2002, 2003; Devincre *et al.*, 2006, 2008; Hansen *et al.*, 2013; Haouala *et al.*, 2018).

The evolution of dislocation density on slip system  $\alpha$  is given by (Dequiedt *et al.*, 2015; Haouala *et al.*, 2018)

$$\dot{\rho}^\alpha = \frac{1}{b} \left( \sqrt{\sum_\beta d^{\alpha\beta} \rho^\beta} - 2r_c \rho^\alpha \right) |\dot{\gamma}^\alpha|. \quad (15)$$

Where  $d^{\alpha\beta}$  is the dislocation multiplication interaction tensor and  $r_c$  is the dislocation capture radius for dislocation annihilation. The tensor  $d^{\alpha\beta}$  is given by the following for self-interacting and coplanar slip systems, with constant  $k_c$

$$d^{\alpha\beta} = \frac{a^{\alpha\beta}}{k_c^2}, \quad (16)$$

and for intersecting non-coplanar systems, with constant  $k_{nc}$

$$d^{\alpha\beta} = \frac{a^{\alpha\beta}}{k_{nc}^2}. \quad (17)$$

The capture radius  $r_c$  for dislocation annihilation is given by the temperature and rate-dependent form based upon work of Kocks (1976)

$$r_c = r_{c0} \left( \frac{|\dot{\gamma}^\alpha|}{\dot{\gamma}_0} \right)^{\frac{k\theta}{A}}. \quad (18)$$

This model was implemented within an ABAQUS UMAT and follows the numerical integration strategy outlined in Kalidindi *et al.* (1992) and Bronkhorst *et al.* (1992). The following section defines the evaluation of the physical quantities in the model for use on the three materials of study in this work.

#### 4. Material Parameter Evaluation

In this section, we outline the procedure used to quantify the list of material parameters used in the model presented in the prior section. The list of quantities and their value are listed in Table 1. The mass density  $\rho$  and specific heat  $c_p$  are both taken as constant for the loading conditions used here and are evaluated from experimental data given in Fig. 9 below. The thermal expansion coefficient  $\alpha$  was measured as explained above in the experimental section and taken as isotropic for a single crystal. The Taylor-Quinney coefficient  $\eta$  was taken as 0.0 for quasi-static rates of loading and 0.95 for rates of loading  $1000 \text{ s}^{-1}$  and greater. Since the elastic constants of stainless steel are very close to those of iron (Boyer and Gall, 1985), the single crystal data for iron from Simmons and Wang (1971) was used to evaluate the temperature relationship for  $C_{11}$ ,  $C_{12}$ , and  $C_{44}$ . The pre-factor  $\dot{\gamma}_0$  in Eq. (9) was taken as  $10^7 \text{ s}^{-1}$  as in Bronkhorst *et al.* (2007). The quantities  $p$  and  $q$ , also from Eq. (9), were taken as 0.33 and 1.66 as guided by the work of Kocks *et al.* (1975). The Hall-Petch type term found in Eq. (14) contains the single quantity  $k_{gr}$  to quantify the grain size influence on mean flow stress for a single crystal. We have used experimental data from the works of Feaugas and Haddou (2003), Kashyap and Tangri (2002), and Singh *et al.* (2002) to estimate this parameter. The experimental data sets from each of the three publications is given in Figs. 6-8. For each of those data sets, the experimental results at a strain of 0.05 was used to evaluate  $k_{gr}$  and is indicated by the red lines in each figure. The value from the work of Feaugas and Haddou (2003) was evaluated to be  $k_{gr} = 31.0 \text{ MPa-mm}^{1/2}$ ; that from Kashyap and Tangri (2002)  $k_{gr} = 5.0 \text{ MPa-mm}^{1/2}$ ; and from Singh *et al.* (2002)  $k_{gr} = 15.2 \text{ MPa-mm}^{1/2}$ .

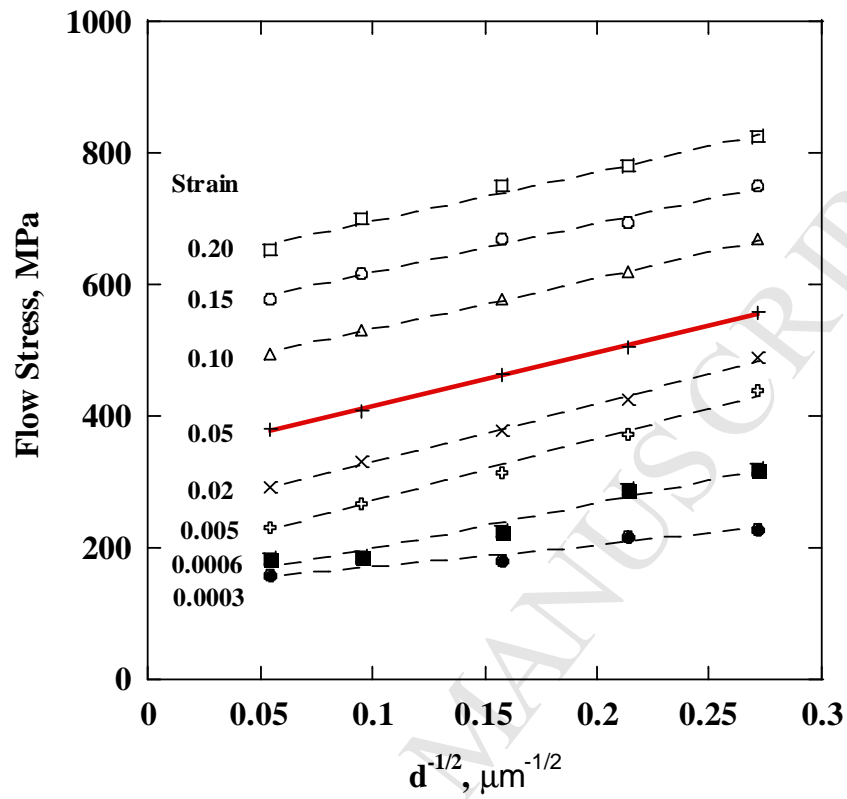


**Fig. 6.** Grain size versus flow stress at different levels of strain from the 316L stainless steel data of Feaugas and Haddou (2003). The red line represents the portion of the experimental dataset which was used for the present study.

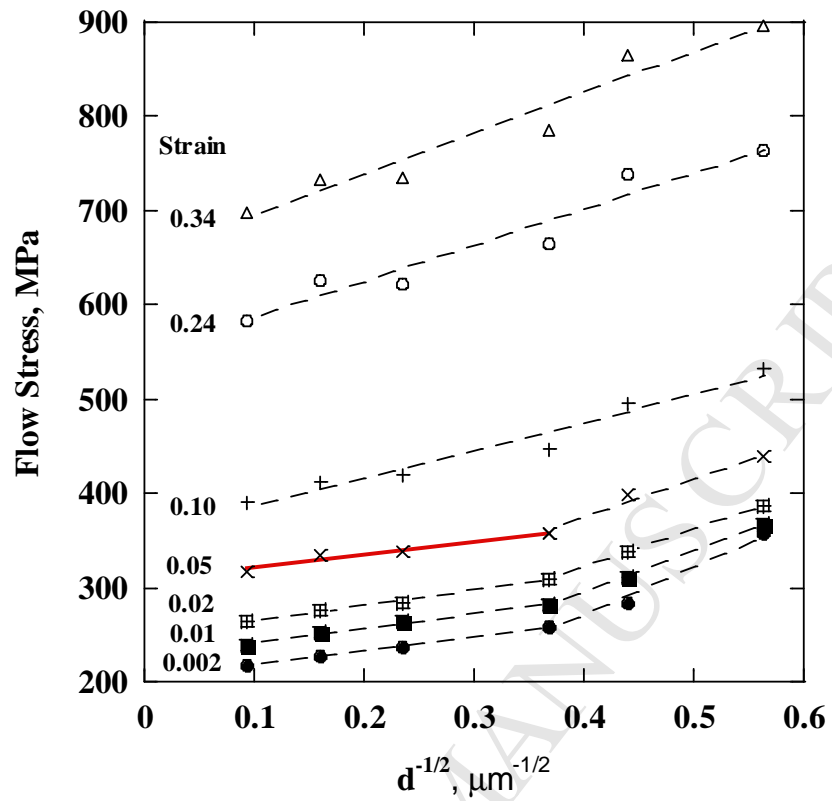


**Fig. 7.** Grain size versus flow stress at different levels of strain from the 316L stainless steel data of Kashyap and Tangri (2002). The red line represents the portion of the experimental dataset which was used for the present study.

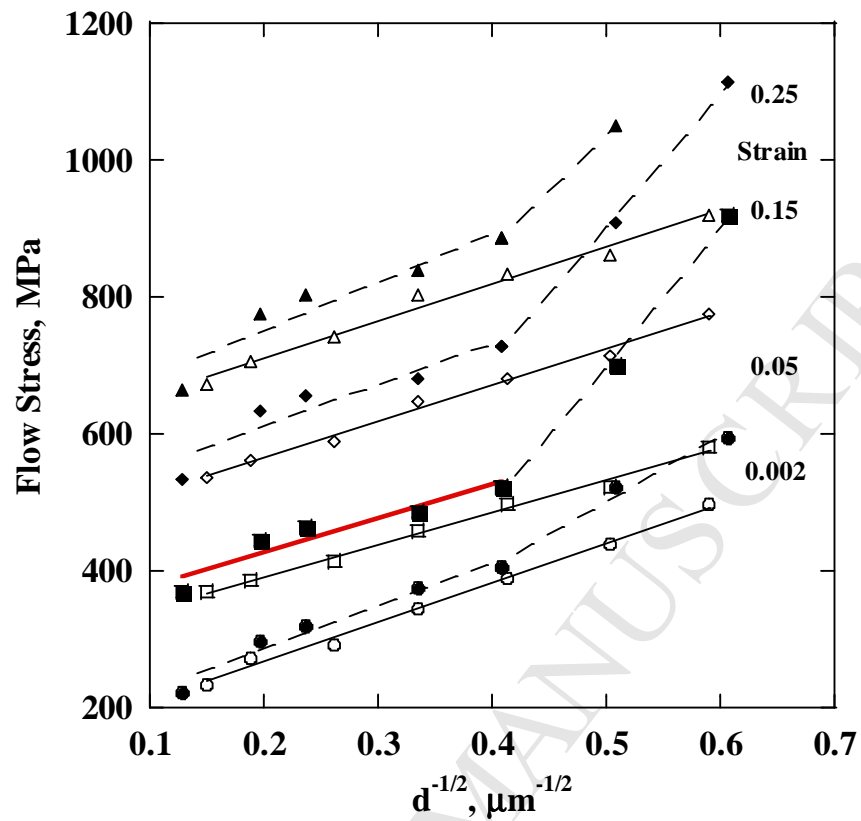


**Fig. 8.** Grain size versus flow stress at different levels of strain from the 316L stainless steel data of Singh *et al.* (2002). The red line represents the portion of the experimental dataset which was used for the present study.

$\rho = 7860 \text{ Kg/m}^3$	$s_l^\alpha = 0.0 \text{ MPa}$
$c_p = 462 \text{ J/kg-K}$	$s_\infty = 0.0 \text{ MPa}$
$\alpha = 16.2 \text{ } \mu\text{m/m-K}$	$\rho_0^\alpha = 9.0 \times 10^7 \text{ 1/mm}^2$
$\eta = 0.0, 0.95$	$k_{gr} = 15.2 \text{ MPa}\sqrt{\text{mm}}$
$m_{11} = -61.63 \text{ MPa/K}$	$b = 2.48 \times 10^{-7} \text{ mm}$
$C_{11_0} = 247.5 \text{ GPa}$	$a_{self} = 0.122$
$m_{12} = -22.7 \text{ MPa/K}$	$a_{dipolar} = 0.122$
$C_{12_0} = 140.3 \text{ GPa}$	$a_{Hirth} = 0.070$
$m_{44} = -23.6 \text{ MPa/K}$	$a_{collinear} = 0.625$
$C_{44_0} = 123.74 \text{ GPa}$	$a_{glissile} = 0.137$
$\dot{\gamma}_0 = 10^7 \text{ sec}^{-1}$	$a_{Lomer} = 0.122$
$F_0 = 7.6 \times 10^{-19} \text{ J}$	$k_c = 6.0$
$p = 0.33$	$k_{nc} = 110.0$
$q = 1.66$	$r_{c0} = 10b$
$d_{gr} = 15.9 \mu\text{m}$	$A = 5.0 \times 10^{-20} \text{ J}$

**Table 1.** Material parameter set used in this study unless indicated otherwise within the manuscript.

The values for the dislocation interaction quantities comprising the tensor  $a_{ij}$  in Eq. (14) were taken directly from the magnitudes reported by Dequiedt *et al.* (2015), Kubin (2013), Madec *et al.* (2002,2003), and Devincre *et al.* (2006,2008). Although there remain some uncertainty to the magnitude of each of these 6 values,  $a_{self}$ ,  $a_{dipolar}$ ,  $a_{Hirth}$ ,  $a_{collinear}$ ,  $a_{glissile}$ ,  $a_{Lomer}$ , the precision with which these quantities are being quantified is continuing to improve. In a similar fashion, the value of capture radius  $r_{c0}$  was taken as the value used by Hansen *et al.* (2013). The intrinsic lattice resistance  $s_l^\alpha$ , for most FCC materials is generally very small so we have assumed that it is zero for this study. In addition, for purposes of this study we have assumed that the long-range resistance  $s_\infty$  is also zero. The values of initial dislocation densities for the three materials are those evaluated experimentally and described above. The initial density for the two annealed materials is taken as  $9.0 \times 10^7 \text{ mm}^{-2}$  while for the as-built AM material is taken as  $2.3 \times 10^8 \text{ mm}^{-2}$ . The remaining 4 quantities, activation energy  $F_0$  from Eq. (9), the dislocation evolution constants  $k_c$  and  $k_{nc}$  from Eqs. (14) and (15) respectively, and capture radius constant  $A$  from Eq. (18) were simultaneously evaluated against experimental uniaxial compression data for 316L stainless steel at differing initial temperatures and strain rates. A cube of 1000 elements with each element a single crystal with assumed initial random crystallographic texture was deformed in uniaxial compression to replicate the experimental conditions. The grain size for these simple compression simulations was taken as the grain size measured on the wrought material for this study with  $d_{gr} = 15.9 \mu\text{m}$  and initial dislocation density of  $9.0 \times 10^7 \text{ mm}^{-2}$ . The resulting

representation of experimental stress strain curves with the completed list of material parameters given in Table 1 is given in Fig. 9.

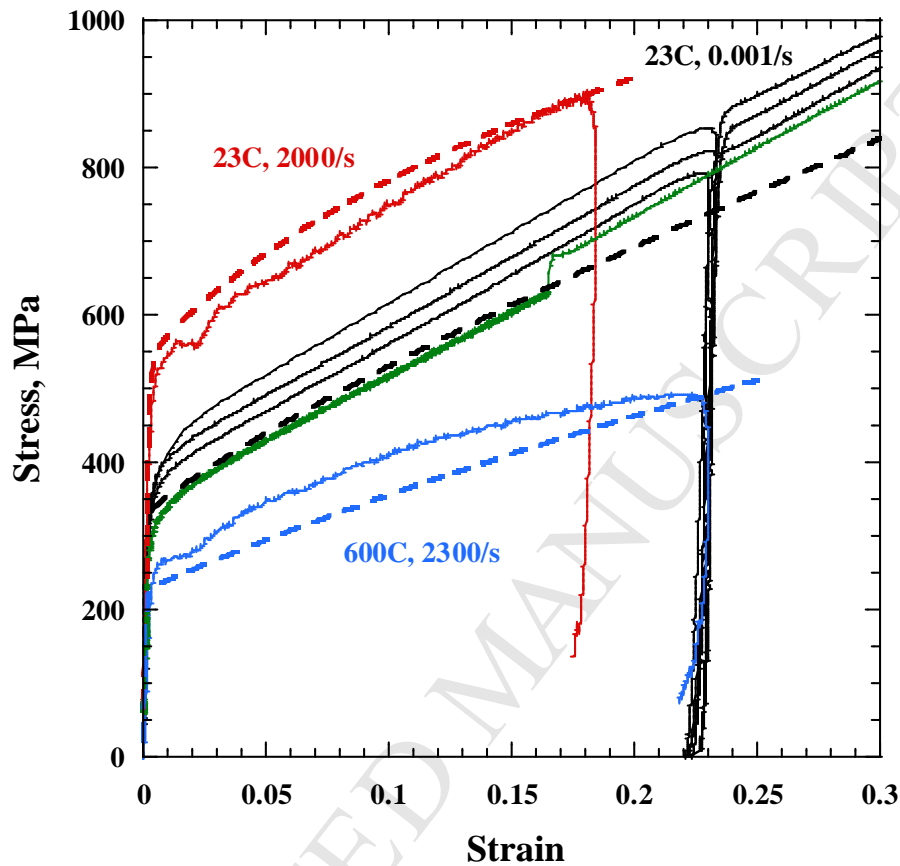


**Fig. 9.** Representation of simple compression experimental data at differing temperature and strain rate conditions for wrought 316L stainless steel. The solid lines are experimental data and the broken lines are simulation results. The red curves represent the conditions of 23 C initial temperature and strain rate of 2000/s. The blue curves represent the conditions of 600 C initial temperature and strain rate of 2300/s. The black curves represent the conditions of 23 C and a strain rate of 0.001/s. The single green curve is from the heat-treated AM material at 23 C and a strain rate of 0.001/s – with a strain rate jump at higher strains which is ignored here.

The experimental data for the wrought material of this study was therefore used as the material for parameter evaluation. There was no input of information from experiments conducted on the as-built AM material nor from the AM material that was heat-treated. In the section that follows, we employ this model to describe the deformation behavior of both the as-built AM and heat-treated AM materials.

## 5. Prediction of Experimental Results and Sensitivity Analysis

In this section, we return our focus to the stress-strain curves given in Fig. 3 where significant differences between the responses of the heat-treated materials and the as-built AM material were observed. In using an advanced model for representation of the 316L material as proposed earlier, it allows for us to provide a physical interpretation of the relative responses of each of the three materials. As already pointed out in the introduction section above, the morphologies of grains produced from AM processes can be quite complex and in stark contrast to our experience with conventionally manufactured materials.

Three EBSD images together with mapped 2D models of each of the microstructures are given in Fig. 10. The colors in the upper row of images indicates crystallographic orientation, however the bottom row colors indicate only individual grains represented by elements. The EBSD sample points in the upper row of images are each defined as a single element in the 2D finite element model. The array of image points is also used to define a two-dimensional grain size for each crystal.

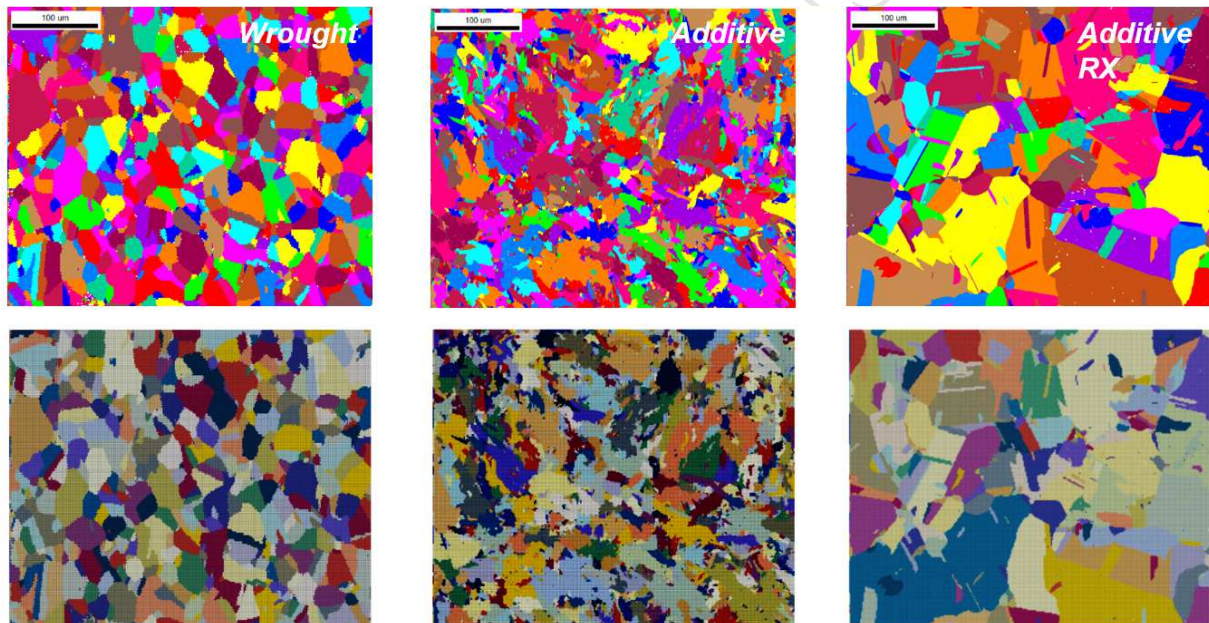


**Fig. 10.** EBSD images (top row) and corresponding two-dimensional mapped models (bottom row) for each of the wrought, as-built additively manufactured, and AM heat-treated materials considered in this study.

Since there are certainly variations in the structure from image to image, we use three different images and construct three different two-dimensional models for each of the three materials to obtain a better estimate of the mechanical response of each material. Each of the EBSD based two-dimensional models displayed in Fig. 10 is constructed into an axi-symmetric compression configuration with the left side representing the centerline of the simulation. Each of the EBSD scan points in the regular scan grid is represented by a single axi-symmetric element CAX4H within ABAQUS. The nodes on the bottom of each image are fixed vertically while allowing for

horizontal displacement. The top line of nodes is prescribed to motion vertically to allow for a true strain rate of  $-0.001 \text{ s}^{-1}$  and allowed to displace horizontally as needed. Consistent with the experiments, an initial temperature of 298K was used for the simulations. The right side line of nodes is unconstrained while the left side edge represents the line of axi-symmetric symmetry. The simulations then are axi-symmetric compression deformation. Grain boundaries are not explicitly represented in these simulations. The grain size is determined for each of the grains in the model and this value of size is used to represent each grain individually. The crystallographic orientation for each grain is also taken to be initially constant. This grain size dependence then is applied to the entire grain equally at each element. The sizes of the grains are scaled so that the mean grain size within each 2D model is consistent with that measured experimentally.

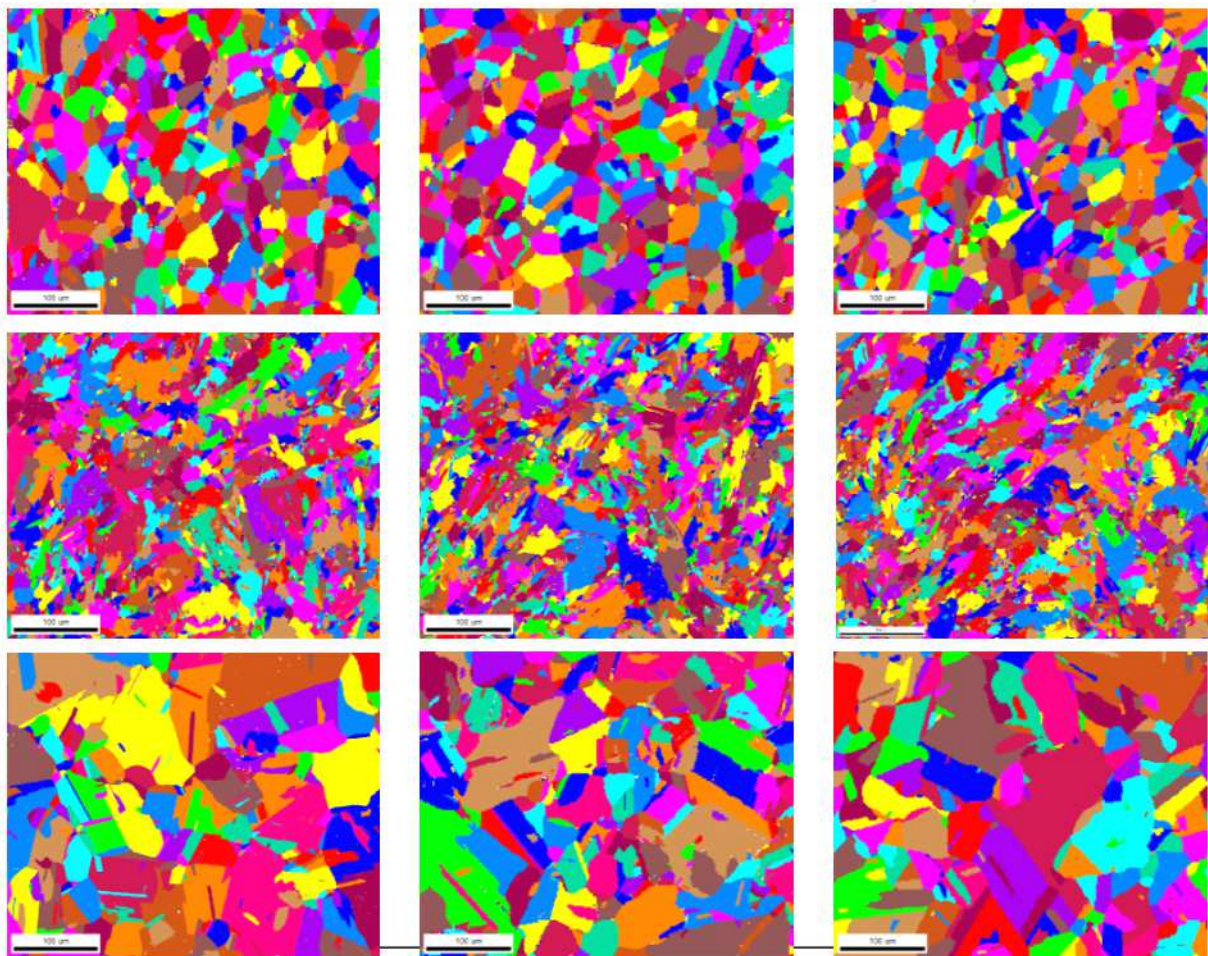


**Fig. 11.** EBSD images of the three different realizations used for numerical simulations for each of the wrought (top row), as-built additively manufactured (center row), and AM heat-treated (bottom row) materials.

The predicted axi-symmetric compression response of the as-built AM and heat-treated AM materials together with the represented response of the wrought material are given in Fig. 12 and

compared directly with the experimental results. In Fig. 12 the dashed lines are those from the simulations while the solid lines are the experimental curves. The simulation results in this figure use the value of the grain size dependence  $k_{gr} = 15.2 \text{ MPa}\cdot\text{mm}^{1/2}$ . The simulation results from the wrought material derive directly from the parameter fitting process and therefore it is not surprising it is represented well. The heat-treated AM material differs from the wrought material in that the grain size is different and this difference is applied to the simulations. The variability of the three microstructures leads to stress-strain curves that display some difference – not seen with the other two materials. The heat-treated AM material results compare quite well with the experimental curves in an average sense. The as-built AM material differs in both mean grain size and also initial dislocation density and displays values of flow stress which are significantly greater at any given strain level than that of the other two materials. This is consistent with the experimental results as well but the calculated results for the as-built AM material are somewhat lower still than the experimental results. Overall however, the predicted results capture well the nature of response of the three materials with differences presumed to arise primarily from differences in grain size and initial dislocation density.

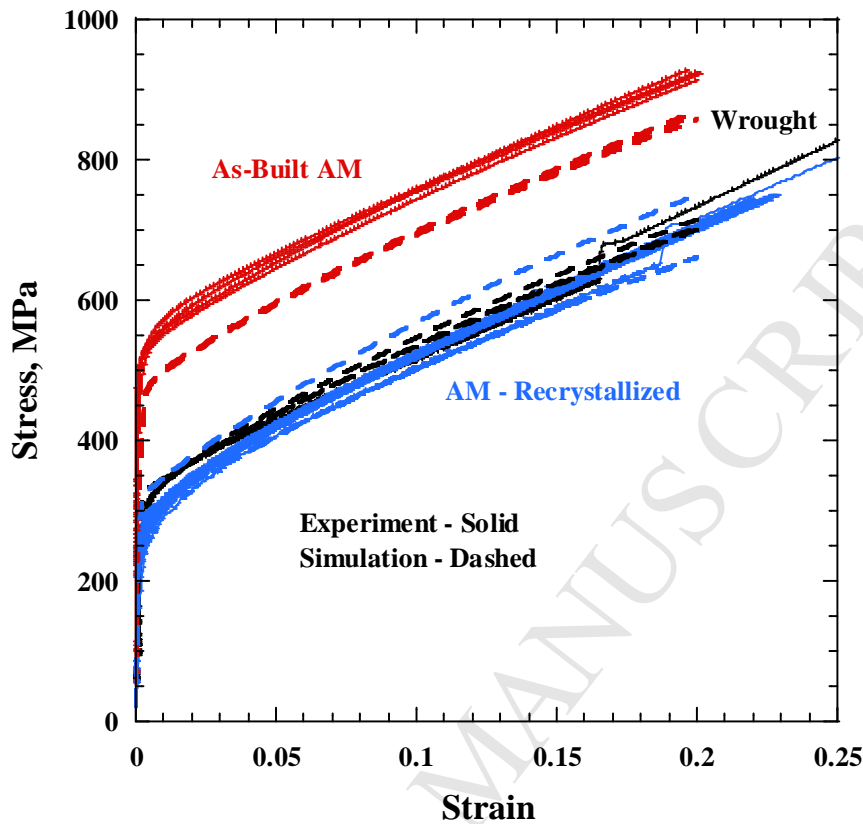


**Fig. 12.** Comparison between predicted and experimental results based upon the axisymmetric simple compression representations using the two-dimensional EBSD images. The solid lines are experimental curves while the broken lines are simulation curves. The red curves represent the as-built AM material. The blue curves represent the heat-treated AM material. The black curves represent the wrought material.

As alluded to in our discussion of the Hall-Petch coefficient  $k_{gr}$  earlier, there is significant uncertainty in the magnitude of the value of this quantity based upon the three sources of experimental information. In addition, as pointed out by the work by Brown et al. (2017) there is also some degree of uncertainty in the ability of line profile analysis work based upon diffraction techniques to discern dislocation density and structure. Both grain size effects and dislocation structure remain topics of intense research. We can however, use what we have with regards to the variability of the information to test the uncertainty in our calculated results. Some simple comparisons are given in Fig. 13 using as our reference the deformation behavior of the as-built AM material for both experiments and the calculation representing the as-built AM material (red curve). The same calculations for the 3 as-built AM models were performed using values of the Hall-Petch coefficient  $k_{gr}$  of  $5.0 \text{ MPa}\cdot\text{mm}^{1/2}$  and  $31.0 \text{ MPa}\cdot\text{mm}^{1/2}$  and are represented by the gold and blue curves respectively in Fig. 13. Using a value of  $k_{gr} = 15.2 \text{ MPa}\cdot\text{mm}^{1/2}$  and increasing the value of initial dislocation density to the point of matching the experimental curves we arrive at a value of  $\rho_0 = 3.1 \times 10^8 \text{ mm}^{-2}$ . This result is given by the green curve overlaying those of the

experiments. This is in comparison to the value of initial dislocation density of  $2.3 \times 10^8 \text{ mm}^{-2}$  used to arrive at the red curve and that used for Fig. 12.

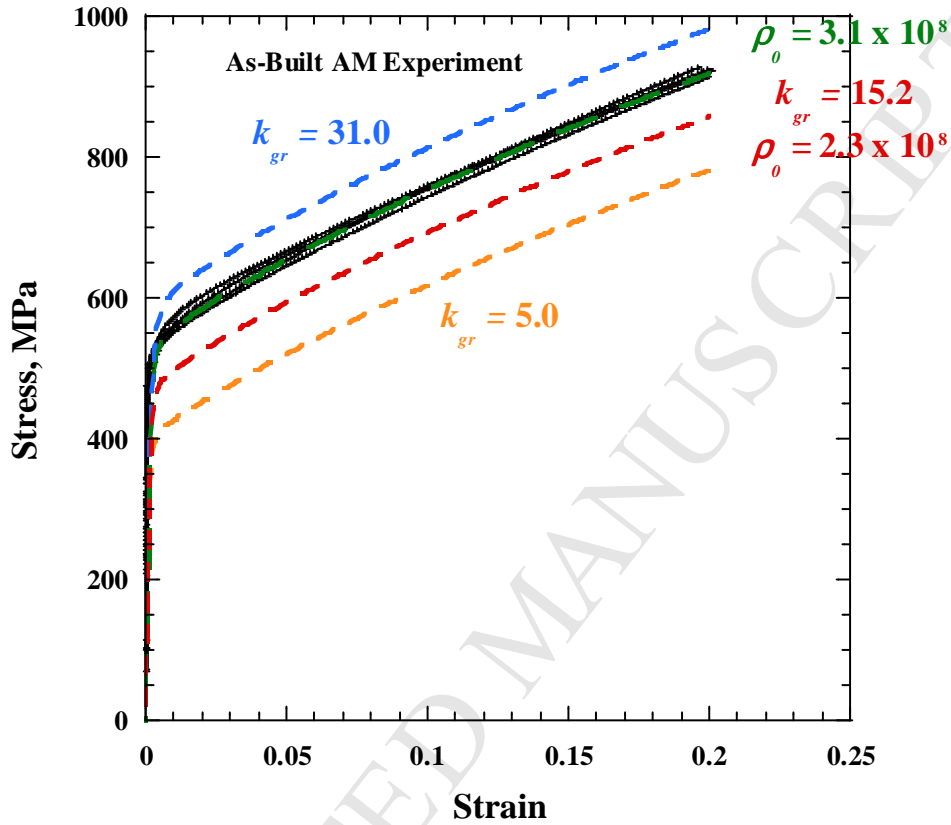


**Fig. 13.** Simulations showing variability of results based upon uncertainties in both representations of initial dislocation density as well as Hall-Petch parameter. The black curves are the experimental curves for the as-built AM material. The broken lines are all simulation results. The blue curve is a simulation using a Hall-Petch parameter value of  $31.0 \text{ MPa}\sqrt{\text{mm}}$ , the red curve a value of  $15.2 \text{ MPa}\sqrt{\text{mm}}$ , and the orange curve  $5.0 \text{ MPa}\sqrt{\text{mm}}$ . The green curve is a simulation using a Hall-Petch parameter value of  $15.2 \text{ MPa}\sqrt{\text{mm}}$  and initial dislocation density of  $3.1 \times 10^8 \text{ mm}^{-2}$ .

The two primary physical features which are prominent here in this work regarding additively manufactured materials is grain size and dislocation structure. The computed results shown in Fig. 14 demonstrate the relative influence of those two factors on the flow stress. The solid red curves are the experimental results for the as-built AM material. The black broken curves are the computed results representing the wrought material and the broken red curves are computed results representing the as-built AM material. Each of these computed results are those used in Fig. 12. For each of the computed results in Fig. 14, a Hall-Petch parameter of  $k_{gr} = 15.2 \text{ MPa}\sqrt{\text{mm}}$  was used. The broken green curves in Fig. 14 are the computed results for the as-built AM material using the initial dislocation density of the wrought material. The broken blue

curves are the computed results for the wrought material using the initial dislocation density of the as-built AM material. Fig. 14 then suggests that within the context of the assumptions made in the model employed here that the primary factor in the increase of flow stress of the as-built AM material is the difference in initial dislocation structure between the wrought and as-built AM materials. Although as the results in Fig. 13 suggest that there is significant uncertainty in the ability of a simple Hall-Petch representation of grain size on flow stress, grain size from current estimates does not appear to be a significant factor. This also is consistent with observations made by Brown et al. (2017) in their study of 304L stainless steel.

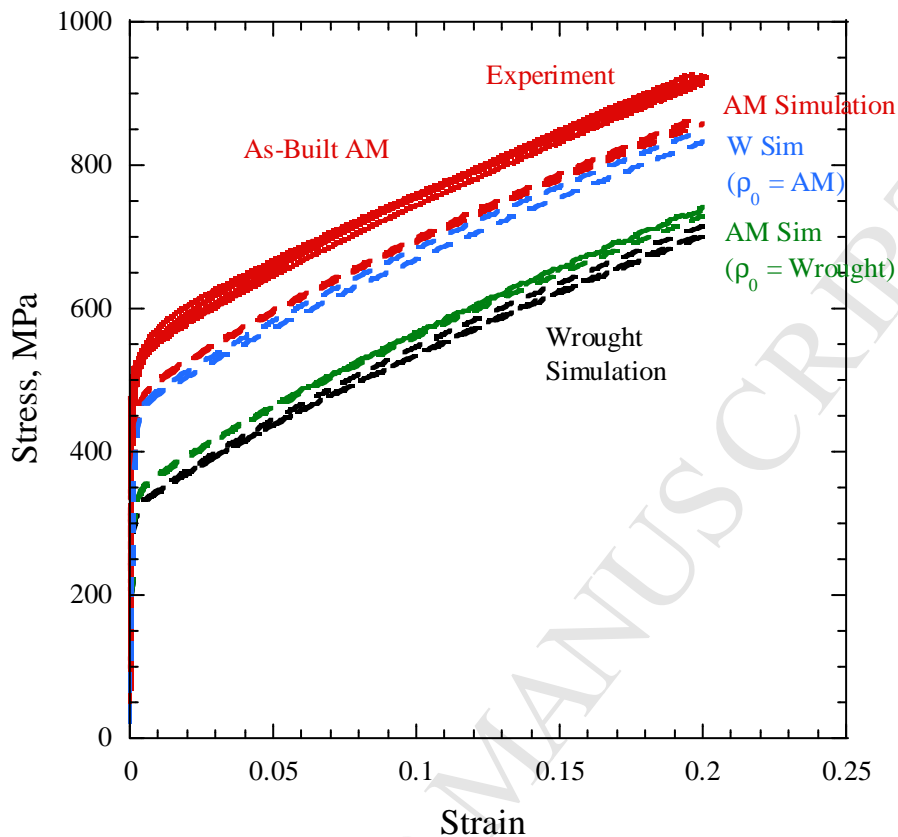


**Fig. 14.** The relative contributions to enhanced flow stress of the additively manufactured material from grain size and dislocation density. The green curves illustrate the effect of grain size relative to the reference of the wrought material. The blue curves illustrate the effect of imposing the dislocation density magnitude of the as-built AM material on the wrought simulations. The broken red curves represent both grain size and greater initial dislocation density. A Hall-Petch parameter of  $k_{gr} = 15.2$  MPa-mm<sup>1/2</sup> was used for all calculations.

## 6. Discussion

Based upon the materials chosen for this study and introduced in section 2 above, it was hypothesized that grain size and initial dislocation structure of the material were the primary factors affecting the flow stress for additively manufactured 316L stainless steel. This hypothesis was built into the model which was proposed in section 4. It is also convenient that the austenitic stainless steels are of FCC structure – for which our ability to represent some of the sophistication of dislocation interactions within a continuum model are the most mature. As discussed in section 5, the evaluation of the physical parameters in the model was done using multiple sources of physical information and represented well the available experimental data. This is not to say however that all uncertainty for FCC materials is eliminated, but rather that we make our assessment of structural performance of these three materials with a model which efficiently represents the prominent characteristics of this class of material in as accurate a way as possible currently.

As the results presented in the previous section suggest, dislocation density is the prominent factor contributing to the substantially higher flow stress for the as-built AM material. Using directly measured estimates of the net dislocation density of the material, we showed that a substantial amount of the increase in plastic flow stress could be predicted with the proposed model. This result is consistent with the results presented by Brown *et al.* (2017) in their work on additively manufactured 304L stainless steel. Fig. 14 in Brown *et al.* (2017) suggests a strong relationship between dislocation density and plastic flow stress of the material manufactured by differing process conditions. Wang *et al.* (2018) examined in detail the structural state of AM produced 316L stainless steel and showed that the as-built material contained a substantial amount of dislocation substructure but also a significant amount of lattice rotation within each grain suggesting the presence of geometrically necessary dislocations (GNDs). They also proposed a single crystal model for representing the grain size and dislocation density of the material and used the characteristic size of the dislocation subcell in their grain size representation for their calculations since it was such a prominent feature in the material. They also presented results that suggested possibilities for material design through manipulation of the structure of the material to enhance mechanical deformation performance. Kapoor *et al.* (2018) examined the feature of strong GND density within as-built Ti-6Al-4V. This alloy contained both HCP  $\alpha$  and BCC  $\beta$  phases as part of the very sophisticated microstructure. The authors proposed and used a deformation rate dependent single crystal model for both phases which accounted for GND populations to study the evolution of internal stress within numerical simulations of representative 2D microstructures. They initialized the as-built internal stress conditions of the material by incorporating the initial GND densities. This work did not however speak to the aggregate deformation behavior via changes in plastic flow stress due to internal stress or structural evolution. This work does illustrate the importance of representing both statistically stored (SS) and GND populations of dislocations for as-built materials at the single crystal level of model development for this small sampling of material examples.

Dislocation line profile analysis (DLPA) is currently the only experimental method that provides bulk dislocation density. In Fig. 12, we observed that the model under-predicted the flow stress for the as-built AM 316L material. The parametric study shown in Fig. 14 suggests that between grain size and dislocations, dislocations play a primary role in contributing to the observed increased flow stress in AM materials. If this is the case, an incorrect initial dislocation density being assumed by the model would explain the model's under-prediction of flow stress. On the other hand, AM materials exhibit hierarchical structure with melt pool sizes of several millimeters and internal substructures of several hundred nanometers (Wang *et al.* (2018)). This hierarchical size effect cannot be captured by a single average grain size value, which is also non-trivial to estimate for AM materials, due to the fact that large intragranular orientation gradients are ubiquitous in AM microstructures. Along with size, grain morphology, and grain boundary types are other microstructural parameters that show significant spatial heterogeneity in AM materials. Grain boundary types and grain shapes are known to influence mechanical properties in conventional materials and could also influence the variation observed in AM material properties. In addition, a 2D microstructural representation does not entirely capture the 3D nature of deformation and microstructure evolution. Although efforts are ongoing to characterize crystallographic 3D microstructures using high-energy X-rays at 3<sup>rd</sup> generation light

sources, the complexity of AM microstructures with large internal deformation and tortuous grain morphology make it challenging to probe 3D microstructures in AM materials.

The question of the influence of initial residual stress internal to the as-built material was not addressed within the theory or calculations presented earlier. We know from the work using diffraction analysis to probe the microstructural state of as-built materials (Brown *et al.*, 2017, 2018; Strantza *et al.*, 2018; Pokharel *et al.*, 2018) that the internal stress implied by lattice distortion has a magnitude that can be on the order of 100's of MPa. The length scale of these measurements is generally large so these measured net residual stress fields are larger than a single weld bead. Based upon measured initial geometrically necessary dislocation density, the work of Kapoor *et al.* (2018) modeled this field and implied a grain level internal stress magnitude. Neither of these studies examined the effect of the internal stress state on the stress-strain response of the as-built material. In an interesting study of prior loading history and its effect on the stress-strain response of 7050 T7 aluminum plate, Barton *et al.* (1999) examined the differences between Sachs, Taylor, and crystal plasticity finite element models. Of particular interest here are the cases in which simulations were conducted by load path changes – tension-compression and tension-shear. This study found that the internal stress formed by the tension cycle effected the duration of the knee of the stress-strain curve upon loading reversal. One might expect that within an as-built component which is externally unloaded that if internal stress exists this must exist so that internally the component balances the tension and compression stress states. Upon application of external loading, one would expect that plastic flow will initiate earlier as the regions with initial stress conditions complementary to those of the externally applied stress would achieve plastic flow first. One would then expect that as loading continues, those regions of the material not complementary to the loading would then reach plastic flow conditions later. The net effect in this thought experiment would then be a stress-strain curve which may display a more extended and larger radius knee in the stress-strain curve as compared to that for a material without residual internal stress.

As pointed out in the introduction, it is possible for other strengthening mechanisms to play a role in changes to flow stress within AM materials. It is expected that chemistry differences and impurities not present in the more traditionally processes materials could provide additional resistance to dislocation motion. These factors were not included in the present quantitative assessment. It is clear from the present work that results suggest that as-built dislocation density and structure play a very large role in the observed elevation of flow stress. It is still too early in our study of as-built AM materials to know how the initial dislocation structure in these materials differ from those induced by simple isothermal deformation. Representing the mechanics of subgrain structure development is still very much a research topic. Certainly the observations of significant populations of geometrically necessary dislocations is a unique feature. This will require sophisticated techniques to initialize computational problems. In addition, it is still important to understand that with any material with an established dislocation structure, we as yet are not able to experimentally distinguish between mobile and immobile portions. There is significant opportunity for detailed computational work to parallel that of quantitative metallography. With the new class of AM materials, the opportunity for more advanced collaborative work is made more urgent given the need to contribute more understanding to the problem of material certification. This also applies to our understanding of grain boundaries and their relationship with mobile dislocations and the relationship between the

grain boundary and their ability to resist the passing of dislocations. The work here does not tangibly represent grain boundaries and therefore we cannot offer any tangible insight into the role that grain boundaries play, however it remains an important question.

The above discussion highlights the point that characterizing as-built materials remains a significant endeavor due to the complexity and variability of microstructures produced. The structures of the materials produced from additive manufacturing processes are new to our experience of modeling materials with certification in mind. Although we have used a simple Hall-Petch representation of the influence of grain size on the flow stress of the single crystals, this is considered to be an oversimplification. Although work demonstrating the influence of grain size on flow stress of many materials has been performed for many years (Cordero *et al.*, 2016), the materials have been traditionally fabricated. The traditional processing techniques generally produce reasonably equiaxed grains and spatial variability of microstructure is generally mild. Since the Hall-Petch expression is very simple and is used to describe empirically based observations, we do not yet know how well such a simple representation will perform applied to as-built additively manufactured materials. The microstructures produced from AM processes can produce very complex topologies (e.g. Gray *et al.*, 2017; Livescu *et al.*, 2018; Wang *et al.*, 2018). The role of grain boundaries affecting flow stress for topologically complex grains remains to be explored at an appropriate level. As we learn more about the details of the structure of the as-built materials, this will also guide us in understanding the types of models necessary to represent them. The work presented here together with that found in literature clearly indicate that process type and process conditions lead to differences in state of the as-built material.

## 7. Conclusion

In this study we have proposed a single crystal model to represent to first order accuracy the physical features hypothesized to be different between as-built AM 316L stainless steel and the same material from traditional wrought processing and heat-treated AM material. These structural feature differences were shown to describe a significant portion of the 1.7 times flow stress difference between the as-built AM material and the other two materials. The 2.5 times higher initial dislocation density in the case of the as-built material over that of the wrought material explained the majority of the flow stress difference. The influence of grain size was shown to be relatively small, however significant variability in the Hall-Petch coefficient was observed based upon literature data for 316L stainless steel manufactured by traditional means. There is also uncertainty in the use of simple Hall-Petch representation of grain size due to the complex topology of grains in as-built AM material. An uncertainty analysis was offered based upon possible variability in our understanding of both grain size and initial dislocation density. This simple analysis suggests that more work is necessary in formulating proper models for the class of as-built AM materials to enable more rapid certification for structural applications.

## Acknowledgements

This work was performed under the auspices of the U.S. DOE under contract DE-AC52-06NA25396. This work was supported by the LANL Advanced Simulation and Computing Program, the LANL Laboratory Directed Research and Development Project 20170033DR, and

by the Exascale Computing Project (17-SC-20-SC), a collaborative effort of the U.S. DOE Office of Science and the NNSA. Fruitful discussions with Dr. S. A. Vander Wiel are gratefully acknowledged.

## References

- Alleman, C., Ghosh, S., Luscher, D. J., Bronkhorst, C. A. (2014). Distribution-enhanced homogenization framework and model for heterogeneous elasto-plastic problems. *J. Mech. Phys. Solids* 85, 176-202.
- AlMangour, B. A. (2017). Additive manufacturing of high-performance 316L stainless steel nanocomposites via selective laser melting. Ph.D. dissertation. University of California Los Angeles.
- Anand, L. (2004). Single-crystal elasto-viscoplasticity: application to texture evolution in polycrystalline metals at large strains. *Comput. Methods Appl. Mech. Engrg.* 193, 5359-5383.
- Asaro, R. J. (1983a). Micromechanics of crystals and polycrystals. *Adv. Appl. Mech.* 23, 1-115.
- Asaro, R. J. (1983b). Crystal plasticity. *J. Appl. Mech.* 50, 921-934.
- Asaro, R. J., Rice, J. R. (1977). Strain localization in ductile single crystals. *J. Mech. Phys. Solids* 25, 309-338.
- Barton, N., Dawson, P., Miller, M. (1999). Yield strength asymmetry predictions from polycrystal elastoplasticity. *ASME J. Engr. Mats. Tech.* 121, April, 230-239.
- Bartolomeu, F., Buciumeanu, M., Pinto, E., Alves, N., Carvalho, O., Silva, F. S., Miranda, G. (2017). 316L stainless steel mechanical and tribological behavior – a comparison between selective laser melting, hot pressing and conventional casting. *Add. Manuf.* 16, 81-89.
- Bonatti, C., Mohr, D. (2017). Large deformation response of additively-manufactured FCC metamaterials: From octet truss lattices towards continuous shell mesostructures. *Int. J. Plasticity* 92, 122-147.
- Boyer, H. E., Gall, T. L. eds. (1985). *Metals Handbook – Desk Edition*. American Society for Metals. Metals Park, OH, USA.
- Bronkhorst, C. A., Kalidindi, S. R., Anand, L. (1992). Polycrystal plasticity and the evolution of crystallographic texture in fcc metals. *Phil. Trans.: Phys. Sci. Engr.* 341, 443-477.
- Bronkhorst, C. A., Hansen, B. L., Cerreta, E. K., Bingert, J. F. (2007). Modeling the microstructural evolution of metallic polycrystalline materials under localization conditions. *J. Mech. Phys. Solids* 55, 2351-2383.

- Brown, D. W., Adams, D. P., Balogh, L., Carpenter, J. S., Clausen, B., King, G., Reedlunn, B., Palmer, T. A., Maguire, M. C., Vogel, S. C. (2017). In situ neutron diffraction study of the influence of microstructure on the mechanical response of additively manufactured 304L stainless steel. *Met. Mats. Trans A* 48, 6055-6069.
- Brown, D. W., Adams, D. P., Balogh, L., Carpenter, J. S., Clausen, B., Livescu, V., Martinez, R. M., Morrow, B. M., Palmer, T. A., Pokharel, R., Strantza, M., Vogel, S. C. (2018). Using in-situ neutron diffraction to isolate specific features of additively manufactured microstructures in 304L stainless steel and identify their effect on macroscopic strength. *Met. Trans. A*, submitted.
- Busso, E. P. (1990). Cyclic deformation of monocrystalline nickel aluminide and high temperature coatings. Ph.D. Thesis, MIT.
- Chen, X., Li, J., Cheng, X., Wang, H., Huang, Z. (2018). Effect of heat treatment on microstructure, mechanical and corrosion properties of austenitic stainless steel 316L using arc additive manufacturing.
- Chen, X., Li, J., Cheng, X., He, B., Wang, H., Huang, Z. (2017). Microstructure and mechanical properties of the austenitic stainless steel 316L fabricated by gas metal arc additive manufacturing. *Mats. Sci. Engr. A* 703, 567-577.
- Cheong, K.-S., Busso, E. P. (2004). Discrete dislocation density modelling of single phase fcc polycrystal aggregates. *Acta Mat.* 52, 5665-5675.
- Dequiedt, J. L., Denoual, C., Madec, R. (2015). Heterogeneous deformation in ductile FCC single crystals in biaxial stretching: the influence of slip system interactions. *J. Mech. Phys. Solids* 83, 301-318.
- Cordero, Z. C., Knight, B. E., Schuh, C. A. (2016). Six decades of the Hall-Petch effect – a survey of grain-size strengthening studies on pure metals. *Int. Mats. Rev.* 61, 491-512.
- Devincre, B., Kubin, L., Hoc, L. (2006). Physical analyses of crystal plasticity by DD simulations. *Scripta Mat.* 54, 741-746.
- Devincre, B., Hoc, T., Kubin, L. (2008). Dislocation mean free paths and strain hardening of crystals. *Science* 320, 1745-1748.
- Feaugas, X., Haddou, H. (2003). Grain-size effects on tensile behavior of nickel and AISI 316L stainless steel. *Met. Mat. Trans. A* 34, 2329-2340.
- Feng, B., Bronkhorst, C. A., Addessio, F. L., Morrow, B. M., Cerreta, E. K., Lookman, T., Lebensohn, R. A., Low, T. (2018). Coupled elasticity, plastic slip, and twinning in single crystal titanium loaded by split-Hopkinson pressure bar. *J. Mech. Phys. Solids* 119, 274-297.
- Francois, M. M., Sun, A., King, W. E., Henson, N. J., Tournet, D., Bronkhorst, C. A., Carlson, N. N., Newman, C. K., Haut, T., Bakosi, J., Gibbs, J. W., Livescu, V., Vander Wiel, S. A., Clarke,

- A. J., Schraad, M. W., Blacker, T., Lim, H., Rodgers, T., Owen, S., Abdeljawad, F., Madison, J., Anderson, A. T., Fattebert, J.-L., Ferencz, R. M., Hodge, N. E., Khairallah, S. A., Walton, O. (2017). Modeling of additive manufacturing processes for metals: challenges and opportunities. *Current Opin. Sol. State Mats. Sci.* 21, 198-206.
- Frazier, W. E. (2014). Metal additive manufacturing: a review. *J. Mats. Engr. Perf.* 23, 1917-1928.
- Gao, W., Zhang, Y., Ramanujan, D., Ramani, K., Chen, Y., Williams, C. B., Wang, C. C. L., Shin, Y. C., Zhang, S., Zavattieri, P. D. (2015). The status, challenges, and future of additive manufacturing in engineering. *Comp.-Aided Design* 69, 65-89.
- Gray III, G. T., Livescu, V., Rigg, P. A., Trujillo, C. P., Cady, C. M., Chen, S. R., Carpenter, J. S., Lienert, T. J., Fensin, S. R. (2017). Structure/property (constitutive and spallation response) of additively manufactured 316L stainless steel. *Acta Mat.* 138, 140-149.
- Grilli, N., Janssens, K. G. F., Nellesen, J., Sandlöbes, S., Raabe, D. (2018). Multiple slip dislocation patterning in a dislocation-based crystal plasticity finite element method. *Int. J. Plast.* 100, 104-121.
- Guo, N., Leu, M. C. (2013). Additive manufacturing: technology, applications and research needs. *Front. Mech. Eng.* 8, 215-243.
- Guo, P., Zou, B., Huang, C., Gao, H. (2017). Study on microstructure, mechanical properties and machinability of efficiently additive manufactured AISI 316L stainless steel by high-power direct laser deposition. *J. Mats. Proc. Tech.* 240, 12-22.
- Gurtin, M. E., Fried, E., Anand, L. (2010). *The mechanics and thermodynamics of continua.* Cambridge University Press, New York, NY.
- Hansen, B. L., Beyerlein, I. J., Bronkhorst, C. A., Cerreta, E. K., Dennis-Koller, D. (2013). A dislocation-based multi-rate single crystal plasticity model. *Int. J. Plast.* 44, 129-146.
- Haouala, S., Segurado, J., Llorca, J. (2018). An analysis of the influence of grain size on the strength of fcc polycrystals by means of computational homogenization. *Acta Mat.* 148, 72-85.
- Hill, R., Rice, J. R. (1972). Constitutive analysis of elastic-plastic crystals at arbitrary strain. *J. Mech. Phys. Solids* 20, 401-413.
- Kalidindi, S. R., Bronkhorst, C. A., Anand, L. (1992). Crystallographic texture evolution in bulk deformation processing of fcc metals. *J. Mech. Phys. Solids* 40, 537-569.
- Kapoor, K., Yoo, Y. S. J., Book T. A., Kacher, J. P., Sangid, M. D. (2018). Incorporating grain-level residual stresses and validating a crystal plasticity model of a two-phase Ti-6Al-4V alloy produced via additive manufacturing. *J. Mech. Phys. Solids* 121, 447-462.

- Kashyap, B. P., Tangri, K. (1995). On the Hall-Petch relationship and substructural evolution in type 316L stainless steel. *Acta Metall. Mat.* 43, 3971-3981.
- Knezevic, M., Beyerlein, I. J. (2018). Multiscale modeling of microstructure-property relationships of polycrystalline metals during thermo-mechanical deformation. *Adv. Engr. Mats.* 20, 1700956.
- Kocks, U. F., Argon, A. S., Ashby, M. F. (1975). *Thermodynamics and kinetics of Slip.* Pergamon Press Ltd.
- Kocks, U. F. (1976). Laws for work-hardening and low-temperature creep. *J. Eng. Mat. Tech.*, January, 76-85.
- Kubin, L. (2013). *Dislocations, mesoscale simulations and plastic flow.* Oxford University Press, Oxford, UK.
- Li, X., Tan, W. (2018). Numerical investigation of effects of nucleation mechanisms on grain structure in metal additive manufacturing. *Comp. Mats. Sci.* 153, 159-169.
- Lim, J. J. H., Malheiros, A. R. C., Bertali, G., Long, C. J., Freyer, P. D., Burke, M. G. (2015). Comparison of additive manufactured and conventional 316L stainless steels. *Microsc. Microanal.* 21.
- Livescu, V., Knapp, C. M., Gray III, G. T., Martinez, R. M., Morrow, B. M., Ndefru, B. G. (2018). Additively manufactured tantalum microstructures. *Materialia* 1, 15-24.
- Lou, X., Song, M., Emigh, P. W., Othon, M. A., Andresen, P. L. (2017). On the stress corrosion crack growth behaviour in high temperature water of 316L stainless steel made by laser powder bed fusion additive manufacturing. *Corr. Sci.* 128, 140-153.
- Lu, W.-Y., Yang, N., Yee, J., Connelly, K. (2018). Mechanical properties of 3-D LENS and PBF printed stainless steel 316L prototypes. In *Mechanics of Additive and Advanced Manufacturing*, volume 9, proceedings of the 2017 Annual Conference on Experimental and Applied Mechanics, chapter 6.
- Madec, R., Devincere, B., Kubin, L. P. (2002). From dislocation junctions to forest hardening. *Phys. Rev. Let.* 89, 255508.
- Madec, R., Devincere, B., Kubin, L., Hoc, T., Rodney, D. (2003). The role of collinear interaction in dislocation-induced hardening. *Science* 301, 1879-1882.
- Martin, J. H., Yahata, B. D., Hundley, J. M., Mayer, J. A., Schaedler, T. A., Pollock, T. M. (2017). 3D printing of high-strength aluminum alloys. *Nature Letters*. DOI: 10.1038/nature23894.

- Marya, M., Singh, V., Marya, S., Hascoet, J. Y. (2015). Microstructural development and technical challenges in laser additive manufacturing: case study with a 316L industrial part. *Met. Mat. Trans. B* 46, 1654-1665.
- Morrow, B. M., Lienert, T. J., Knapp, C. M., Sutton, J. O., Brand, M. J., Pacheco, R. M., Livescu, V., Carpenter, J. S., Gray III, G. T. (2018). Impact of defects in powder feedstock materials on microstructure of 304L and 316L stainless steel produced by additive manufacturing. *Met. Mat. Trans. A* 49, 3637-3650.
- Nishida, E., Song, B., Maguire, M., Adams, D., Carroll, J., Wise, J., Bishop, J., Palmer, T. (2015). Dynamic compressive response of wrought and additive manufactured 304L stainless steels. *EPJ Web of Confs.* 94, DOI: 10.1051/epjconf/20159401001.
- Pace, M. L., Guarnaccio, A., Dolce, P., Mollica, D., Parisi, G. P., Lettino, A., Medici, L., Summa, V., Ciancio, R., Santagata, A. (2017). 3D additive manufactured 316L components microstructural features and changes induced by working life cycles. *Appl. Surface Sci.* 418, 437-445.
- Pham, M. S., Dovggy, B., Hooper, P. A. (2017). Twinning induced plasticity in austenitic stainless steel 316L made by additive manufacturing. *Mats. Sci. Engr. A* 704, 102-111.
- Pokharel, R., Balogh, L., Brown, D. W., Clausen, B., Gray III, G. T., Livescu, V., Vogel, S. C., Takajo, S. (2018). Signatures of the unique microstructure of additively manufactured steel observed via diffraction, *Scripta Mat.* 155, 16-20.
- Pokharel, R., Lebensohn, R. A. (2018). Instantiation of crystal plasticity simulations for micromechanical modelling with direct input from microstructural data collected at light sources, *Scripta Mat.* 132, 73-77.
- Rännar, L.-E., Koptyug, A., Olsén, J., Saeidi, K., Shen, Z. (2017). Hierarchical structures of stainless steel 316L manufactured by electron beam melting. *Add. Manuf.* 17, 106-112.
- Ribarik, G., Gubicza, J., Ungar, T. (2004). Correlation between strength and microstructure of ball-milled Al-Mg alloys determined by X-ray diffraction. *Mat. Sci. Engr. A* 387-389, 343-347.
- Rice, J. R. (1971). Inelastic constitutive relations for solids: an internal-variable theory and its application to metal plasticity. *J. Mech. Phys. Solids* 19, 433-455.
- Simmons, G., Wang, H. (1971). *Single Crystal Elastic Constants and Calculated Aggregate Properties: A Handbook*. MIT Press, Cambridge, MA.
- Simson, T., Emmel, A., Dwars, A., Böhm, J. (2017). Residual stress measurements on AISI 316L samples manufactured by selective laser melting. *Add. Manuf.* 17, 183-189.
- Singh, K. K., Sangal, S., Murty, G. S. (2002). Hall-Petch behavior of 316L austenitic stainless steel at room temperature. *Mats. Sci. Tech.* 18, 165-172.

Strantz, M., Ganeriwala, R. K., Clausen, B., Phan, T. Q., Levine, L. E., Pagan, D., King, W. E., Hodge, N. E., Brown, D. W. (2018). Coupled experimental and computational study of residual stresses in additively manufactured Ti-6Al-4V components. *Mats. Lett.* 231, 221-224.

Tapia, G., Khairallah, S., Matthews, M., King, W. E., Elwany, A. (2017). Gaussian process-based surrogate modeling framework for process planning in laser powder-bed fusion additive manufacturing of 316L stainless steel. *Int. J. Adv. Manuf. Technol.*, DOI 10.1007/s00170-017-1045-z.

Wang, H., Capolungo, L., Clausen, B., Tomé, C. N. (2017). A crystal plasticity model based on transition state theory. *Int. J. Plasticity* 93, 251-268.

Wang, Y. M., Voisin, T., McKeown, J. T., Ye, J., Calta, N. P., Li, Z., Zeng, Z., Zhang, Y., Chen, W., Roehling, T. T., Ott, R. T., Santala, M. K., Depond, P. J., Matthews, M. J., Hamza, A. V., Zhu, T. (2018). Additively manufactured hierarchical stainless steels with high strength and ductility. *Nature Materials*. DOI: 10.1038/NMAT5021.

Wang, Z., Palmer, T. A., Beese, A. M. (2016). Effect of processing parameters on microstructure and tensile properties of austenitic stainless steel 304L made by directed energy deposition additive manufacturing. *Acta Mat.* 110, 226-235.

Wu, A. S., Brown, D. W., Kumar, M., Gallegos, G. F., King, W. E. (2014). An experimental investigation into additive manufacturing – induced residual stresses in 316L stainless steel. *Met. Mats. Trans A* 45, 6260-6270.

Yadollahi, A., Shamsaei, N., Hammi, Y., Horstemeyer, M. F. (2016). Quantification of tensile damage evolution in additive manufactured austenitic stainless steels. *Mats. Sci. Engr. A* 657, 399-405.

Yang, N., Yee, J., Zheng, B., Gaiser, K., Reynolds, T., Clemon, L., Lu, W. Y., Schoenung, J. M., Lavernia, E. J. (2017). Process-structure-property relationships for 316L stainless steel fabricated by additive manufacturing and its implication for component engineering. *J. Therm. Spray Tech.* 26, 610-626.

Zhong, Y. (2017). Sub-grain structure in additive manufactured stainless steel 316L. Ph.D. dissertation. Stockholm University, Sweden.

Zhong, Y., Rännar, L.-E., Liu, L., Koptuyug, A., Wikman, S., Olsen, J., Cui, D., Shen, Z. (2017). Additive manufacturing of 316L stainless steel by electron beam melting for nuclear fusion applications. *J. Nucl. Mats.* 486, 234-245.